Journal of Solid State Chemistry 183 (2010) 2372–2381

Contents lists available at ScienceDirect

Journal of Solid State Chemistry

journal homepage: www.elsevier.com/locate/jssc

Structure alterations in microporous $(Mg,Fe)_2Al_4Si_5O_{18}$ crystals induced by energetic heavy-ion irradiation

Ronald Miletich [a,*], G. Diego Gatta [b], Günther J. Redhammer [c], Michael Burchard [a], Hans-Peter Meyer [a], Christian Weikusat [a,d], Nicola Rotiroti [b], Ulrich A. Glasmacher [a], Christina Trautmann [d], Reinhard Neumann [d]

[a] Institut für Geowissenschaften, Universität Heidelberg, Im Neuenheimer Feld 234-236, D-69120 Heidelberg, Germany
[b] Dipartimento di Scienze della Terra, Università degli Studi di Milano, Via Botticelli 23, I-20133 Milano, Italy
[c] Fachbereich Materialforschung und Physik, Abteilung Mineralogie, Universität Salzburg, Hellbrunnerstrasse 34, A-5020 Salzburg, Austria
[d] GSI Helmholtzzentrum für Schwerionenforschung, Materials Research, Planckstrasse 1, D-64291 Darmstadt, Germany

ARTICLE INFO

Article history:
Received 28 April 2010
Received in revised form
21 July 2010
Accepted 22 July 2010
Available online 30 July 2010

Keywords:
Cordierite
Microporous framework structure
MeV heavy ions
Ion-beam induced colouration
Irradiation-induced dehydration

ABSTRACT

The microporous framework structure of $(Mg_{1-x}Fe_x)_2Al_4Si_5O_{18}$ (=cordierite) has been subject to a comparative study on the effect of structural alterations originating from exposure to high-energy heavy ions. Oriented samples (with $x=0.061$, 0.122, and 0.170) were irradiated with swift ^{124}Xe, ^{197}Au and ^{96}Ru ions with 11.1 MeV per nucleon energy and fluences of 1×10^{12} and 1×10^{13} ions/cm^2. Irradiated and non-irradiated samples were investigated by means of X-ray diffraction, Mössbauer spectroscopy and optical absorption spectroscopy. Structural investigations reveal an essentially unchanged Al,Si ordering, which appears to be unaffected by irradiation. The most remarkable macroscopic change is the ion-beam induced colouration, which could be assigned to electronic charge transfer transitions involving the Fe cations. Mössbauer spectra indicate an increased amount of $^{[4]}Fe^{3+}$ for the irradiated sample. The most noticeable structural alteration concerns irradiation-induced dehydration of extra-framework H_2O, which is accompanied by a reduction in the molar volume by ~0.2 vol%.

1. Introduction

The magnesium–aluminium cyclosilicate $Mg_2Al_4Si_5O_{18}$ has received considerable attention as a dielectric due to its superior thermomechanical properties, in particular the low thermal expansivity [1–4] and the low dielectric constants [5]. Ceramics with a large portion of $Mg_2Al_4Si_5O_{18}$ component found widespread commercial use as thermal insulators or catalytic converters, showing high mechanical strength at elevated temperatures and good mechanical resistance to thermal shock due to large temperature gradients or temperature changes on a short timescale. A further striking feature concerns the optical properties of crystals. In particular the macroscopic color and the distinct pleochroism of Fe-bearing $(Mg_{1-x}Fe_x)_2Al_4Si_5O_{18}$ solid-solutions between end-member $Mg_2Al_4Si_5O_{18}$ (=cordierite) and $Fe_2Al_4Si_5O_{18}$ (=sekaninaite) makes natural "iolite" being a prominent gemstone material. Moreover, optical properties of cordierite ceramics have gained considerable importance in the development of precision optics and ceramic optical components [6]. The unique properties to sustain extraordinary ambient conditions makes cordierite ceramics and composite materials getting into the focus of aerospace and military industry, in particular plasma-sprayed coatings [7] and fibrous composite materials [8,9]. Regarding relativistic particles and high-energetic radiation for ambient conditions as considerably extreme, the motivation for this study here can be easily understood with respect to the growing importance of cordierite materials adopted for use in aerospace and nuclear technology.

Investigations on the structure–property relations of $(Mg,Fe)_2Al_4Si_5O_{18}$ under extraordinary conditions concentrated in particular on the variations at changing temperature conditions. One major focus is the temperature-related order/disorder phase transition related to the Al,Si-distribution within the $(Al,Si)_6O_{18}$ ring units [10–14], which is accompanied by a symmetry change from *Cccm* (cordierite) to *P*6/*mcc* (indialite) space-group symmetry [10,15]. The mechanisms and details of the cation ordering associated with the cordierite-to-indialite transformation at ~1750 K have been subject to numerous studies (e.g. [12,16–18]). Apart from the Al,Si-ordering on tetrahedral sites, a large number of investigations related to the Fe^{2+},Fe^{3+}-site occupation was performed in order to shed light on the structural origins of optical absorption properties and pleochroism [19–26]. Due to the framework nature (Fig.1), the microporous $(Mg,Fe)_2Al_4Si_5O_{18}$ structure incorporates in addition volatile molecular species, most prominently H_2O and CO_2 among

* Corresponding author. Fax: +49 6221 544805.
E-mail address: ronald.miletich@geow.uni-heidelberg.de (R. Miletich).

0022-4596/$ - see front matter © 2010 Elsevier Inc. All rights reserved.
doi:10.1016/j.jssc.2010.07.038

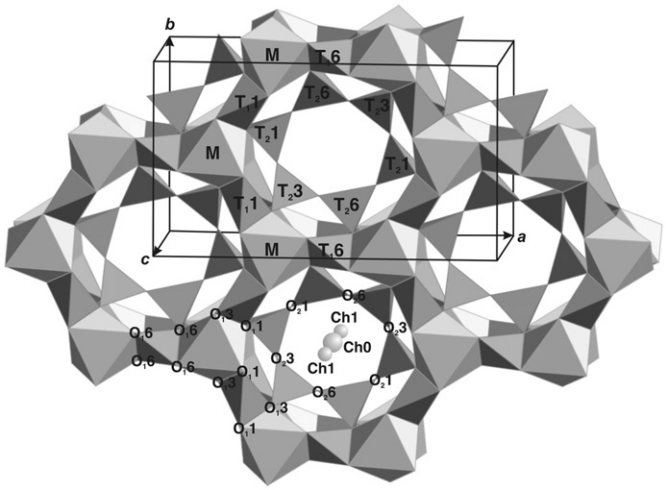

Fig. 1. Structural configuration and site assignments in $(Mg,Fe)_2Al_4Si_5O_{18}$ (space group *Cccm*, $a \approx 17.1$, $b \approx 9.7$, $c \approx 9.3$ Å) visualized in a polyhedral model viewed along the crystallographic [0.1 0.3 2.3] zone-axis direction. The site assignment follows [18].

molecular nitrogen, noble gases and even simple hydrocarbons in natural samples [21,27–33]. Moreover, natural crystals are also subject to significant substitutions by Be^{2+} and Li^{+} on the M- and T-sites of the framework, which in turn explains charge compensations by extra-framework alkali ions inside the cavities of the six-membered $(Al,Si)_6O_{18}$ silicate rings [34–36]. Accordingly, the compositional variations of natural cordierite can be described best by $^{Ch}(Na,K,Ca,Cs)_{\leq 1}\,[^{[6]}(Mg,Fe^{2+},Mn,Li)_2^{[4]}(Si,Al,Be,Fe^{3+})_9O_{18}]\cdot{}^{Ch}(H_2O, CO_2,CO,N_2,Ar,\ldots)_{\leq 1}$. A significant part of the detailed knowledge about the structural chemistry originates from a series of structure-related investigations carried out over many years (e.g. [10,16–19,22,25,28–30,37–53]).

Due to the outstanding physical properties the investigations on $(Mg,Fe)_2Al_4Si_5O_{18}$ structural behaviour under extreme conditions have been extended to various natural and artificial radiation exposures by γ-rays, α-particles, and more recently also by high-energy heavy ions [22,54–57]. One major motivation for previous irradiation studies originates from understanding the formation of yellowish-brown pleochroitic α-particle haloes in natural host cordierites around actinide-bearing mineral inclusions, and the structural alterations associated with the radiation damage. All studies reveal a low degree of structural radiation damage, and amorphization only to occur in a few nanometer distances away from the interface to the inclusion phase. Moreover, the polarization characteristics of band positions in the optical absorption spectra measured within the area of radiocoloration suggest electronic transitions related to electron color centres at Frenkel defects. Radiocoloration appears to be independent of the type of irradiation or masses of particles. Previous studies by means of Raman spectroscopy indicate irradiation-induced changes of the quantity and the nature of species of extra-framework molecular volatiles [55,57]. Results from the latter studies suggested the irradiation-induced loss of H_2O and the conversion of molecular CO from CO_2 to correlate with the differential energy loss along the path of the incident ions.

Artificial irradiation with MeV–GeV heavy ions has the major advantage that a significant volume of a given sample can be modified in a controlled manner by adjusting the ion energy, the penetration depth of ions, and the applied fluence. This facilitates the application of analytical techniques to measure also bulk properties of larger crystal portions, which were irradiated under controlled homogeneous conditions. Here we employ single-crystal X-ray diffraction (XRD) in order to investigate the crystal structures of homogeneously irradiated and non-irradiated samples. Mössbauer spectroscopy and optical absorption spectroscopy add to the comparative crystal-structure investigations through XRD. The aim of this study is to validate the radiation-induced alterations of the crystal structure of $(Mg,Fe)_2Al_4Si_5O_{18}$ from a crystallographic point of view.

2. Materials and methods

2.1. Sample crystals

Experiments were carried out on oriented samples prepared from 3 cm-size pale-blue translucent natural crystals of gemstone quality (“iolite”) from Mount Tsilaizina, Madagascar (sample denotation “Tsi1”, “Tsi2” and “Tsi3”). All three specimens were cut perpendicular to the crystallographic axes (following the setting $a \approx 17.1$, $b \approx 9.7$, and $c \approx 9.3$ Å) giving rectangular cuboids and truncated fragments of random orientation. The crystal orientation was determined within a precision of about 0.3° by means of optical microscopy and X-ray diffraction film methods. In addition to one-sided polished sections of the truncated crystals of random orientation, double-sided polished oriented thin sections according to the (100), (010), (001) orientations were prepared from the cuboids. The thickness of almost all crystal platelets was below 100 μm and thus smaller than the calculated penetration depth of the ion beams; lateral dimensions of the platelets range between ~3 and 5 mm. All double-sided polished crystal sections were examined under crossed polarizers to check for twinning, section growths, mineral inclusions, lattice imperfections, and mechanically induced macroscopic defects.

2.2. Crystal compositions

The composition of the three crystals was determined using electron microprobe (EMP) analysis. The determination of the light elements (Li, Be, B) was carried out by using secondary-ion mass spectrometry (SIMS). Truncated crystal fragments were embedded in epoxy resin, ground and polished, sputtered with carbon for EMP analyses and with gold for SIMS investigations. Line-scan profiles across the samples reveal ideal homogeneous composition without any indication for heterogeneities. Analyses of the major elements were performed using a Cameca SX-51 electron microprobe equipped with five wavelength-dispersive spectrometers and an energy-dispersive spectrometer. Operating conditions were 15 kV accelerating voltage, 20 nA beam current and 20 s counting time for all elements and PAP correction [58] was applied to the raw data. The presence of Li, Be, and B was determined by SIMS using a Cameca IMS 3*f* ion microprobe equipped with a primary-beam mass filter. Analyses were performed using a 14.5 kV/20 nA $^{16}O^{-}$ primary-ion beam. Secondary-ion intensities of ^{7}Li, ^{9}Be, and ^{11}B were normalized to the count rate of ^{30}Si and calibrated against the glass reference NIST SRM610 [59]. The analytical results from EMP and SIMS analyses are summarized in Table 1. H_2O and CO_2 contents were derived following the method described by Kaindl et al. [60] from the corresponding vibrational modes in Raman spectra [57], which give ~0.7–0.9 wt% H_2O and ~0.4–0.5 wt% CO_2. The chemical formulae of the sample specimens correspond to $Na_{0.026}[(Mg_{0.892}Fe_{0.123})_2Al_{3.984}Si_{4.987}O_{18}](H_2O)_{0.45}(CO_2)_{0.07}$ (=Tsi1); $Na_{0.031}[(Mg_{0.952}Fe_{0.062})_2Al_{3.995}Si_{4.979}O_{18}](H_2O)_{0.54}(CO_2)_{0.04}$ (=Tsi2), and $Na_{0.019}[(Mg_{0.839}Fe_{0.172})_2\ Al_{3.985}Si_{4.992}O_{18}](H_2O)_{0.47}(CO_2)_{0.04}$ (=Tsi3).

2.3. Ion-irradiation experiments

The exposure of samples to swift heavy ions (^{96}Ru, ^{124}Xe, ^{197}Au) was carried out at the UNILAC linear accelerator of *GSI Helmholtzzentrum für Schwerionenforschung*. All irradiation experiments were performed in vacuum at ambient temperature applying fluences ϕ of 1×10^{12} and 1×10^{13} ions/cm^2, following the results described by Weikusat et al. [57]. The irradiation of samples was carried out with the ion-beam direction perpendicular to the oriented crystallographic faces. To avoid sample heating, the beam intensity was limited to about 10^8 ions/cm^2 s. The penetration depth and energy loss of the ions were calculated with the SRIM2006 code [61]. The mean energy loss (initial kinetic energy divided by ion range) is 12 keV/nm (^{96}Ru), 15 keV/nm (^{124}Xe) and 25 keV/nm (^{197}Au). By defocusing, the ion beam is sufficiently broad providing homogeneous irradiation conditions over the entire sample area. According to both the calculated electronic energy loss dE/dx and observed intensity variations of Raman modes in line scans perpendicular to the surface [55,57], the radiation damage varies only by about 20% up to a depth of ~65–75 μm for Ru, ~70–80 μm μm for Xe, and to ~90–100 μm μm for Au ions. The experimental conditions and individual irradiation parameters are summarized in Table 2.

Table 1
Chemical composition of the $(Mg_{1-x}Fe_x)_2Al_4Si_5O_{18}$ (Tsi1: $x=0.122$; Tsi2: $x=0.061$; Tsi3: $x=0.170$) single-crystal specimen used for this study. Numbers in parentheses represent the uncertainties.

	Tsi1	Tsi2	Tsi3
SiO_2	50.00(20)	50.00(24)	49.87(25)
Al_2O_3	33.89(11)	34.04(10)	33.78(9)
FeO	2.96(7)	1.48(6)	4.11(10)
MnO	0.02(1)	0.03(2)	0.05(2)
MgO	12.00(7)	12.83(7)	11.25(7)
CaO	0.01(1)	0.01(1)	0.01(1)
Na_2O	0.14(2)	0.16(2)	0.10(2)
K_2O	0.02(1)	0.03(1)	0.01(1)
Σ	99.03(29)	98.58(28)	99.17(38)
Li	19.4(2)	22.9(2)	n.d.
Be	20.8(2)	15.1(5)	n.d.
B	<1	7.9(2)	n.d.
Mg	1.784(9)	1.905(10)	1.678(10)
Fe	0.247(6)	0.123(5)	0.344(9)
Mn	0.002(1)	0.003(2)	0.004(2)
Li	0.001	0.002	n.d.
$\Sigma_{[6]}$	2.034	2.033	2.026
Al	3.984(10)	3.995(15)	3.985(14)
Si	4.987(9)	4.979(13)	4.992(15)
Be	0.001	0.002	n.d.
B	<0.001	<0.001	n.d.
$\Sigma_{[4]}$	8.972	8.976	8.977
$\Sigma_{[4]}+\Sigma_{[6]}$	11.006	11.009	11.003
Na	0.026(3)	0.031(3)	0.019(3)
K	0.002(2)	0.004(1)	0.001(1)
Ca	0.001(1)	0.001(1)	0.001(1)

Note: Oxide contents are given in wt%, contents of Li, Be, and B in μg/g. Standard deviations are derived from 45 to 48 individual EMP analyses, those for Li, Be, B from three individual SIMS analyses. The contents of TiO_2, Cr_2O_3, ZnO, and NiO were below the detection limits. Formula coefficients were calculated on the basis of 18 oxygen atoms without considering the extra-framework H_2O and CO_2 inside the channels.

2.4. Single-crystal X-ray diffraction

Single-crystal XRD investigations were performed on irradiated and non-irradiated fragments from the samples Tsi1 ($x=0.122$), Tsi2 ($x=0.061$), and Tsi3 ($x=0.170$). Lattice parameters in total of six crystals were determined at ambient conditions on a *Huber* 5042 four-circle diffractometer using non-monochromatized Mo-radiation from a sealed-tube source (35 kV/25 mA operation power). The setting angles of 17–20 diffracted Bragg peaks between 13.3 and 22.8° 2θ, were recorded with a point detector, using motorized slits with settings of 2 and 9 mm for the scan directions within and perpendicular to the diffraction plane, and employing the method of eight-position diffracted-beam centering [62]. Fittings of reflection profiles considered the $\alpha_1-\alpha_2$ peak splitting using constraints for the position and intensity ($\alpha_2/\alpha_1=0.53$) of the α_2-peak components as implemented in the *SINGLE04* software [63]. The results of symmetry-constrained vector-least squares refinements are listed in Table 3a. Intensity data, aimed at the structural refinements, were collected from samples Tsi2#R_n ($\phi=0$) and Tsi2#R_i ($\phi=1\times10^{13}$) at room conditions with a *Xcalibur Oxford Diffraction* diffractometer equipped with a CCD detector, using a graphite-monochromatized Mo$K\alpha$-radiation (operated at 50 kV/40 mA). A combination of ω and φ scans was used in order to maximize the reciprocal space coverage and redundancy, with a step size of 0.4° and an exposure time of 20 s/frame. The distance between the crystal and the detector was fixed to 80 mm. The diffraction data were collected in the range $2<2\theta<72.7°$. Lorentz-polarization, analytical absorption corrections, and data reduction according to Laue class *mmm* were performed using the *CrysAlis* package [64]. The reflection conditions were consistent with the space group *Cccm*. Details of the data collection and results of structure refinements are summarized in Table 3b.

Table 2
Sample material and parameter for individual swift heavy-ion irradiation experiments.

Sample	Tsi1#R_i	Tsi2#R_i	Tsi3#C_a1i Tsi3#C_a2i Tsi3#C_ci	Tsi2#C_ai Tsi2#C_bi Tsi2#C_ci	Tsi1#C_ci
Sample crystal					
Cut ⊥	n.d.	n.d.	a, b, c	a, b, c	c

Thickness (μm)	3.5×10^3	110 ± 3	//a: 88 ± 3
			//b: 75 ± 3
			//c: 70 ± 3
				//a: 78 ± 3
				//b: 76 ± 3
				//c: 58 ± 3
					//c: 65–70

Beamtime	09/2007	08/2008	08/2008	02/2009	03/2009
Ion species	^{124}Xe	^{197}Au	^{197}Au	^{197}Au	^{96}Ru
Energy (MeV/u)	11.1	11.1	11.1	11.1	11.1
Fluence ϕ (cm^{-2})	1×10^{12}	1×10^{13}	1×10^{13}	1×10^{12}	1×10^{12}

Sample denotation: Three crystal specimen (Tsi1, Tsi2, Tsi3), from which truncated crystal fragments with random orientation (#R) or crystallographically cut cuboids (#C) were fabricated with finally oriented faces perpendicular to the *a*-, *b*- or *c*-axis (_a, _b, _c). The letter "i" indicates sample irradiation; Tsi1#R refers to the sample used by Armbruster and Bloss [29], which contains an irradiated layer in direct contact with the non-irradiated crystal.

Table 3a
Lattice parameters of the three samples of $(Mg_{1-x}Fe_x)_2Al_4Si_5O_{18}$ (Tsi1: $x=0.122$; Tsi2: $x=0.061$; Tsi3: $x=0.170$). Δ represents the lattice distortion index with $\Delta=1.904(a-b\sqrt{3})$ as derived from the lattice parameters a and b, according to Selkregg and Bloss [74].

Tsi1#R,	$\phi=0$	1×10^{12} Xe/cm^2
a (Å)	17.0719(4)	17.0682(8)
b (Å)	9.7224(3)	9.7176(7)
c (Å)	9.3489(2)	9.3360(8)
V (Å^3)	1551.74(6)	1548.48(16)
Δ	0.2533	0.2591
Tsi2#R,	$\phi=0$	1×10^{13} Au/cm^2
a (Å)	17.0738(4)	17.0639(5)
b (Å)	9.7193(4)	9.7158(4)
c (Å)	9.3451(3)	9.3354(4)
V (Å^3)	1550.78(8)	1547.71(9)
Δ	0.2619	0.2578
Tsi3#C_c,	$\phi=0$	1×10^{13} Au/cm^2
a (Å)	17.0960(5)	17.0869(6)
b (Å)	9.7348(4)	9.7299(5)
c (Å)	9.3368(4)	9.3286(4)
V (Å^3)	1553.89(9)	1550.92(11)
Δ	0.2569	0.2562

Table 3b
Details of crystals from sample Tsi2 used for single-crystal diffraction, parameters of the XRD intensity measurements and data of the structure refinements.

Tsi2#R,	$\phi=0$	1×10^{13} Au/cm^2
Crystal size (μm)	$110\times140\times210$	$115\times160\times220$
μ (mm^{-1})	0.94	1.05
a (Å)	17.076(1)	17.068(1)
b (Å)	9.735(1)	9.718(1)
c (Å)	9.341(1)	9.336(1)
V (Å^3)	1552.9(2)	1548.5(2)
max. $\pm h$, $\pm k$, $\pm l$	28, 12, 15	28, 13, 14
No. of refls.	20,873	20,701
No. of unique refls.	1641	1698
With $F_o>4\sigma(F_o)$	1264	1357
No. of parameters	87	87
R_{int}	0.0601	0.0473
R_1 $F_o>4\sigma(F_o)$	0.0266	0.0236
R_1 $F_o>0\sigma(F_o)$	0.0470	0.0406
wR_2	0.0461	0.0413
GooF	1.008	1.176
δe_{max} /Å^3	0.48	0.56
δe_{min} /Å^3	−0.58	−0.51

2.5. Structure refinements

The structural refinements were conducted with anisotropic displacement parameters using the *SHELX-97* software [65], starting from the atomic coordinates given by Cohen et al. [27] and using neutral atomic scattering factors for Mg, Al, Fe, Si, O, and Na from the *International Tables for X-ray Crystallography* [66]. Mixed scattering curves with (Mg+Fe) at the octahedral M site and with (Al+Si), (Al+Fe) and (Si+Fe) at the various tetrahedral $T_1$1, $T_1$6, $T_2$1, $T_2$6 and $T_2$3 sites were used in refinements. The first cycles of the anisotropic refinements were performed without any extra-framework atoms. Difference-Fourier summation (Fig. 2) reveals two maxima of the electron density at 0,0,1/4 (=Ch1/4 site) and 0,0,0 (=Ch0 site), which were assigned to the Na-site and to the oxygen atom of the water molecule. In the final difference-Fourier summation no electron densities larger than ±0.5 and $\pm0.6\,e^-$/Å^3 were present for the non-irradiated and irradiated crystal, respectively. A careful inspection of the difference-Fourier functions did not show any evidence of additional CO_2 sites as reported by Malcherek et al. [49]. The use of mixed scattering curves at the tetrahedral $T_1$1, $T_1$6, $T_2$6 and $T_2$3 sites did not improve the figures of merit of the refinements: $T_1$1 and $T_2$6 were found to be fully occupied by Al, whereas $T_1$6, $T_2$1 and $T_2$3 were found to be fully occupied by Si. Refinements did not give evidence for significant amounts of Fe on any of the tetrahedral sites, whereas the refinement of the site-occupation factors of the M site revealed significant but meaningless differences with respect to the presumably true (Mg,Fe) occupation. The final refinements were carried out with anisotropic displacement parameters U_{ij} for all framework atoms and with U_{iso} for the extra-framework atoms. The resulting positional and displacement parameters and refined site occupation factors are listed in Table 4. Table 5 comprises selected interatomic distances according to the final refinements and gives bond valences calculated after Brese and O'Keeffe [67].

2.6. Mössbauer spectroscopy

Transmission ^{57}Fe Mössbauer spectra were collected at room temperature using a Mössbauer apparatus (*Halder electronics*, Germany) in horizontal arrangement (^{57}Co/Rh single-line thin source, constant acceleration mode, symmetric triangular velocity shape, multi-channel analyser with 1024 channels, velocity scale calibrated to α-iron). For the absorber preparation in a first series of experiments, thin single-crystal slabs of non-irradiated and irradiated samples (Tsi3#C_ci, Tsi3#C_cn, 3 mm lateral diameter, 80 μm mm thickness) were fixed onto sticky tape, which was glued into Cu-rings (inner diameter 10 mm and covered with a high-purity Al-foil on one side). The area of the absorber not covered with the sample was masked with a thin Pb-foil. In a second series of experiments non-irradiated and irradiated samples (four platelets of Tsi1#C_ci and one Tsi1#R_n crystal fragment) were carefully ground under ethanol, filled into the Cu-rings, and mixed with powder sugar to fix the sample. The folded spectra were analyzed using full static Hamiltonian site analysis (using Lorentzian shaped doublets), as implemented in the program code *RECOIL* [68,69].

2.7. Optical absorption spectroscopy

Unpolarized optical absorption spectra were measured on three irradiated samples in comparison to the three non-irradiated crystal sections, each with the crystallographic orientation //(100), (010) and (001). The spectra were recorded with a circular measuring spot of 1 mm diameter in the range 190–900 nm (54,000–11,000 cm^{-1}). The measurements were performed at a double beam UNICAM UV4 spectrometer at a fixed spectral resolution of 2 nm using a halogen lamp source. Background (in air) and sample spectra were averaged from three scans.

3. Results and discussion

3.1. Lattice properties

Both the peak shapes in XRD profiles and the small errors for the lattice parameters reveal that ion irradiation does not affect considerably the long-range order within the crystal. The peak widths fitted from ω-scans yield values between 0.16° and 0.19° for the irradiated samples, which is almost identical with the values obtained from the scans of the non-irradiated sample (0.13–0.17°). The observation is in accordance with the low degree of radiation-induced lattice defects for the area inside the

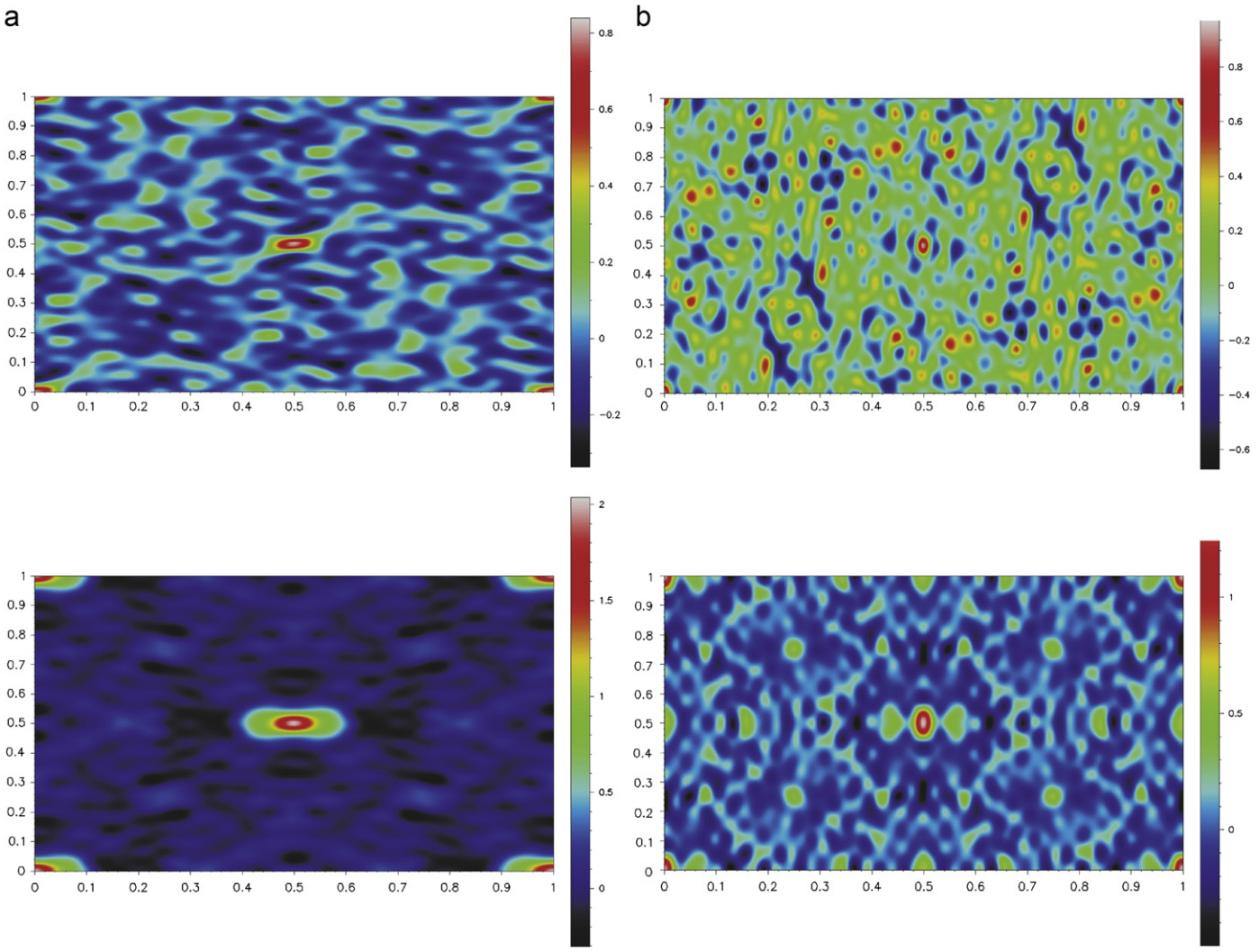

Fig. 2. Difference Fourier maps of the electron density ($e^-/Å^3$) of (a) non-irradiated and (b) irradiated cordierite at $z=0$ (above) and $z=1/4$ (below) based on refinement without the sodium and the water molecule sites, showing positive residual peaks at 0,0,0 (ascribable to sodium, Ch0) and 0,0,1/4 (ascribable to water, Ch1/4). (Note: the color scale is different for the two maps; map orientation: *a* positive to the right).

natural radiohaloes [54]. Our findings from the diffraction patterns account for an evidently undisturbed long-range order, lack of any significant crystal mosaicity, and the absence of structural or compositional gradients and associated strain within the sample crystals due to spatial inhomogeneous irradiation.

On the other hand, the obtained values for the orthorhombic base vectors reveal, independent of the degree of (Mg↔Fe) substitution, a decrease of the lattice dimensions for all samples in all three crystallographic axes (*a*-axis: −0.47‰ to −0.58‰, *b*-axis: −0.36‰ to −0.79‰, *c*-axis: −0.57‰ to −1.04‰). The corresponding volume difference of −2.8 to −3.1 $Å^3$ yields a relative volume change by −1.84‰ to −1.98‰. These findings are completely opposite to the observations in many low-dielectric materials, where irradiation with heavy ions in the MeV to GeV energy regime induces pronounced volume expansion (e.g. [70,71]). In amorphizable oxide phases so-called lattice swelling is in agreement with a change of the density related to the volume fraction of the amorphized cylindrical zones, which are created along the trajectories of the energetic ions. Lattice strain associated with the volume expansion in these amorphous tracks would be manifested by a significant increase of the FWHM of lattice-related signals, which could not be observed for the investigated samples. Large-scale amorphization, which was described to occur either at very high fluences [72] or under the electron beam [73], can be excluded.

Both the optical properties as observed under crossed polarizers and the values of measured lattice parameters confirm that the orthorhombic symmetry remains unchanged even after exposure to the highest ion fluence of 1×10^{13} cm^{-2}. The lattice distortion index Δ (as derived from $\Delta=1.094(a-b\sqrt{3})$ [74]), which is a measure for the orthorhombic distortion from the ideal hexagonal framework geometry, is not affected significantly comparing the lattice dimensions of the irradiated and non-irradiated crystals. Earlier investigations revealed the distortion index Δ to increase with temperature, water pressure, Al,Si ordering and with decreasing contents of channel constituents [29,39,51,75]. The marginal changes due to the irradiation do not evidence any significant changes of the orthorhombic distortion resulting from the exposure of the crystals to swift heavy ions.

3.2. Irradiation effect on the framework structure

The framework structure corresponds to $(M)_2(T_16)(T_11)_2[(T_23)_2(T_21)_2(T_26)_2O_{18}]$, following earlier site assignments [27] for the octahedral (M) and different tetrahedral (T) sites (cf. also

Table 4

Atomic coordinates and displacement parameters ($Å^2 \times 10^4$). U_{eq} is defined as one-third of the trace of the orthogonalized U_{ij} tensor. The exponent of the anisotropic displacement factor takes on the form: $-2\pi^2[h^2a^{*2}U_{11}+\cdots+2hka^*b^*U_{12}]$. Atomic sites in space group *Cccm* correspond to 4*a* (Ow), 4*b* (T_16), 4*c* (Na), 8*g* (M), 8*k* (T_11), 8*l* (T_21, T_23, T_26, O_26, O_21, O_23), and 16*m* (O_11, O_16, O_13). The site occupancy factors of M, T_11, T_16, T_21, T_23, T_26, Ch 1/4 and Ch 0 site were refined.

Site	Occupancy	*x*/*a*	*y*/*b*	*z*/*c*	U_{11}	U_{22}	U_{33}	U_{23}	U_{13}	U_{12}	U_{eq}
Tsi2#R, non-irradiated, $\phi=0$											
M	$Mg_{0.971(3)}Fe_{0.029(3)}$	0.16260(3)	0	1/4	53(3)	60(4)	81(3)	0(2)	0	0	64(2)
T_11	$Al_{0.968(3)}$	1/4	1/4	0.25015(5)	68(3)	52(3)	57(3)	0	0	13(2)	59(2)
T_16	$Si_{0.959(4)}$	0	0.5	1/4	39(3)	53(4)	48(3)	0	0	0	47(2)
T_21	$Si_{0.966(3)}$	0.19261(2)	0.07799(5)	0	44(2)	40(3)	52(3)	0	0	3(2)	45(2)
T_23	$Si_{0.968(3)}$	−0.13519(2)	0.23732(5)	0	42(2)	46(3)	56(3)	0	0	−7(2)	48(2)
T_26	$Al_{0.946(4)}$	0.05080(3)	0.30791(5)	0	77(3)	86(3)	91(3)	0	0	8(2)	85(2)
O_11	$O_{1.00}$	0.24729(5)	0.10312(8)	0.14108(9)	115(4)	83(5)	89(4)	−10(3)	−26(3)	11(3)	96(2)
O_16	$O_{1.00}$	0.06223(4)	0.41615(8)	0.15105(8)	80(4)	117(5)	90(4)	−29(3)	0(3)	7(3)	96(2)
O_13	$O_{1.00}$	−0.17323(4)	0.31006(8)	0.14145(9)	100(4)	98(5)	90(4)	−22(3)	17(3)	−16(3)	96(2)
O_26	$O_{1.00}$	−0.04304(6)	0.24768(13)	0	66(5)	163(7)	178(7)	0	0	−12(5)	136(3)
O_21	$O_{1.00}$	0.12243(7)	0.18462(12)	0	112(5)	114(7)	170(7)	0	0	39(5)	132(3)
O_23	$O_{1.00}$	−0.16459(7)	0.07961(13)	0	137(6)	88(6)	172(6)	0	0	−26(5)	132(3)
Ch 1/4	$Ow_{0.78(2)}$	0	0	1/4	366(17)						
Ch 0	$Na_{0.047(6)}$	0	0	0	30(10)						
Tsi2#R, irradiated, $\phi=1\times10^{13}$ Au/cm^2											
M	$Mg_{0.911(3)}Fe_{0.089(3)}$	0.16258(2)	0	1/4	50(3)	68(3)	91(3)	2(2)	0	0	69(4)
T_11	$Al_{0.983(3)}$	1/4	1/4	0.25003(5)	67(2)	64(3)	64(3)	0	0	15(2)	65(2)
T_16	$Si_{0.982(4)}$	0	0.5	1/4	44(3)	70(3)	55(3)	0	0	0	57(2)
T_21	$Si_{0.976(3)}$	0.19239(2)	0.07797(3)	0	42(2)	44(2)	57(3)	0	0	2(2)	48(2)
T_23	$Si_{0.981(3)}$	−0.13511(2)	0.23716(3)	0	40(2)	55(2)	60(2)	0	0	−9(2)	52(2)
T_26	$Al_{0.956(3)}$	0.05076(2)	0.30771(4)	0	69(3)	96(3)	90(3)	0	0	7(2)	85(2)
O_11	$O_{1.00}$	0.24713(4)	0.10294(6)	0.14121(8)	112(4)	90(4)	90(4)	−7(3)	−29(3)	7(3)	97(2)
O_16	$O_{1.00}$	0.06215(4)	0.41610(6)	0.15113(7)	74(3)	117(4)	89(4)	−28(3)	−5(3)	10(3)	93(2)
O_13	$O_{1.00}$	−0.17328(4)	0.30982(7)	0.14161(8)	92(3)	107(4)	94(4)	−21(3)	20(3)	−14(3)	98(2)
O_26	$O_{1.00}$	−0.04330(6)	0.24830(10)	0	68(5)	171(5)	173(6)	0	0	−17(4)	137(3)
O_21	$O_{1.00}$	0.12239(6)	0.18457(10)	0	96(5)	116(5)	195(6)	0	0	45(4)	136(3)
O_23	$O_{1.00}$	−0.16431(6)	0.07953(9)	0	133(5)	80(5)	180(6)	0	0	−31(4)	131(3)
Ch 1/4	$Ow_{0.43(2)}$	0	0	1/4	257(17)						
Ch 0	$Na_{0.030(6)}$	0	0	0	47(18)						

Fig.1). It reveals a clear relationship to the hexagonal indialite-type $(M)_2(T_1)_3[(T_2)_6O_{18}]$ framework, which is well represented by the isomorphous $Al_2Be_3[Si_6O_{18}]$ (=beryl structure). While the distribution of Be^{2+} and Si^{4+} in hexagonal beryl is clearly assigned to the $3T_1$ and $6T_2$ positions, the distribution of 4 Al+5 Si in cordierite requires ordering of Si and Al atoms, symmetry breaking from *P*6/*mcc* to *Cccm*, and involves an order–disorder phase transition at the critical temperature $T_c \sim 1750$ K [13,17,18,44,76,77]. Our results from structure refinements (Tables 4 and 5) reveal equivalent site-occupancy distributions for the respective tetrahedral position corresponding to fully ordered $SiAl_2[Si_2Si_2Al_2O_{18}]$ framework arrangement. Ion-induced temperature spikes originating from the energy deposition of the swift heavy ions are discussed within community using high-energy ions for material modification, but direct evidence for surpassing the critical temperature of the order–disorder transition cannot be verified due to the short time scales ($< 10^{-10}$ s) involved. Moreover, the lattice parameters *a* and *b* as well as the remaining orthorhombic distortion clearly support that the experimental conditions of heavy-ion irradiation do not provoke a significant change in the existing bulk Al,Si ordering.

With respect to the Fe distribution between M and T sites, the observed electron densities of the T sites suggest no or only insignificant Fe contents on the T sites according to the refinements with mixed (Al+Fe) and (Si+Fe) scattering curves, which corresponds to earlier findings reporting that only minor amount of Fe^{3+} substitutes for Al on the T_11 site [24–26]. These studies suggest that Fe^{3+} is located almost exclusively on tetrahedral sites, following the substitution mechanisms $^{[4]}Al^{3+}+{}^{Ch}\square = {}^{[4]}Fe^{2+}+{}^{Ch}Na^{+}$ and $^{[4]}Si^{4+}+{}^{Ch}\square = {}^{[4]}Fe^{3+}+{}^{Ch}Na^{+}$ involving both ferrous and ferric species [24,34,35]. Referring to effects originating from experiments with ionizing radiation, none of the previous studies considered the role of vacancies within the framework, and the charge compensation by valence change from Fe^{2+} to Fe^{3+}. The single-crystal Mössbauer spectrum of the non-irradiated crystal slab of sample Tsi3#c_cn is dominated by an asymmetric quadrupole doublet (due to the single crystal nature of the slab), arising from ferrous iron in octahedral coordination ($^{[6]}Fe^{2+}$ with isomer shift $\delta = 1.21 \pm 0.01$ mm/s and quadrupole splitting $\Delta = 2.32 \pm 0.01$ mm/s). These values agree with those given in literature [22,25]. A detailed inspection of the spectrum exhibits a very small amount of ferric iron with a doublet given by the hyperfine parameters $\delta = 0.18 \pm 0.01$ mm/s and $\Delta = 0.62 \pm 0.03$ mm/s, which are somewhat different to those given by Geiger et al. [25], but they are consistent with Fe^{3+} in tetrahedral coordination. The Mössbauer spectrum of the powdered non-irradiated crystal fragment (sample Tsi1#R_n, Fig. 3a) is dominated by $^{[6]}Fe^{2+}$ ($\delta = 1.210 \pm 0.006$ mm/s and $\Delta = 2.343 \pm 0.009$ mm/s) very close to the ones of the single-crystal slab. Additionally, there are clear evidences for $^{[4]}Fe^{2+}$ as probed by weak shoulders on the low velocity sides of the $^{[6]}Fe^{2+}$ absorption lines. The relative area fraction is $4.0 \pm 0.8\%$ of total iron, the hyperfine parameters ($\delta = 0.93 \pm 0.03$ mm/s, $\Delta = 2.33 \pm 0.04$ mm/s) generally meet those given by Vance and Price [22]. In addition small amounts $3.2 \pm 0.6\%$ of the total iron content appearing as $^{[4]}Fe^{3+}$ also are present ($\delta = 0.20 \pm 0.02$ mm/s and $\Delta = 0.59 \pm 0.05$ mm/s). The Mössbauer spectrum of the powdered four irradiated crystal platelets of sample Tsi#1 reveals a somewhat altered appearance (Fig. 3b): evidences for $^{[4]}Fe^{2+}$, e.g. a shoulder at Doppler velocities of ~ -0.4 mm/s are no longer visible, thus no doublet was fitted, while a significantly more intense ferric iron component is now visible at Doppler velocities of $\sim +0.5$ mm/s. The hyperfine parameters ($\delta = 0.13 \pm 0.02$ mm/s and $\Delta = 0.54 \pm 0.05$ mm/s) suggest an assignment to $^{[4]}Fe^{3+}$, the relative fraction is $14.9 \pm 1.8\%$. The corresponding hyperfine parameters for $^{[6]}Fe^{2+}$ are identical to the ones in the non-irradiated sample within

Table 5
Calculated bond distances (Å) and bond valences s (v.u.) after Brese and O'Keeffe [67] in irradiated (1×10^{13} Au/cm^2) and non-irradiated ($(Mg_{0.939}Fe_{0.061})_2Al_4Si_5O_{18}$.

ϕ (Au/cm^2)	0		1×10^{13}	
M (Mg,Fe) 2..				
$-O_11$ ($\times2$)	2.1002(8)	0.337	2.0993(7)	0.337
$-O_16$ ($\times2$)	2.1116(8)	0.330	2.1108(7)	0.329
$-O_13$ ($\times2$)	2.1167(8)	0.322	2.1149(7)	0.322
$\langle M–O\rangle$, Σs	2.1095	1.978	2.1083	1.976
T_11(Al) ..2				
$-O_13$ ($\times2$)	1.7566(8)	0.755	1.7538(7)	0.758
$-O_11$ ($\times2$)	1.7564(6)	0.749	1.7541(7)	0.759
$\langle T_11–O\rangle$, Σs	1.7565	3.008	1.7539	3.034
T_16(Si) 222				
$-O_16$ ($\times4$)	1.6278(8)	0.987	1.6254(6)	0.992
Σs		3.948		3.967
T_21(Si) ..m				
$-O_21$	1.5855(12)	1.099	1.5813(10)	1.109
$-O_23$	1.6072(13)	1.056	1.6038(10)	1.068
$-O_11$ ($\times2$)	1.6335(8)	0.970	1.6339(7)	0.970
$\langle T_21—O\rangle$, Σs	1.6149	4.095	1.6032	4.117
T_23(Si) ..m				
$-O_26$	1.5769(12)	1.151	1.5709(10)	1.160
$-O_23$	1.6154(13)	1.017	1.6108(10)	1.029
$-O_13$ ($\times2$)	1.6338(9)	0.966	1.6343(7)	0.972
$\langle T_23–O\rangle$, Σs	1.6150	4.101	1.6126	4.133
T_26(Al) ..2				
$-O_26$	1.7063(12)	0.856	1.7061(10)	0.858
$-O_21$	1.7137(13)	0.845	1.7108(10)	0.840
$-O_16$ ($\times2$)	1.7718(8)	0.717	1.7714(7)	0.721
$\langle T_26–O\rangle$, Σs	1.7409	3.135	1.7399	3.140
Ch0(Na) ..2/m				
$-O_w$ ($\times2$)	2.3353(2)	0.235	2.3340(2)	0.236
$-O_26$ ($\times2$)	2.5208(13)	0.141	2.5235(10)	0.139
$-O_21$ ($\times2$)	2.7570(12)	0.075	2.7534(10)	0.076
$-O_23$ ($\times2$)	2.9155(12)	0.049	2.9091(10)	0.050
Σs		1.000		1.002

experimental error ($\delta=1.213\pm0.007$ mm/s and $\Delta=2.330\pm0.013$ mm/s).

Optical absorption spectra for the three main crystal directions, comparing irradiated (ai, bi, ci) and non-irradiated (an, bn, cn) samples, are shown in Figs. 4 and 5. While the non-irradiated sample platelets are apparently colorless in the given thickness, the irradiated crystal platelets exhibit a macroscopically visible change to faint yellow color for all three orientations. Similar to the spectroscopic findings observed for radiocoloration in alpha-particle haloes [54], we observe a strong red-shift of the absorption edge from the ultraviolet (UV) towards the onset of the visible spectral region. A broad absorption band, which is centred at ~22,000 cm^{-1} dominates the visible spectrum for E//*c* [54] and can be confirmed in the spectra "ai" and "bi", while it is absent in the spectrum obtained for "ci". In addition to the well-known Fe^{2+} *d–d* transitions in the NIR region (8000–11,000 cm^{-1}), two weak and broad intensities centred at ~18,300 and ~21,200 cm^{-1} can be observed (Fig. 5), which suggest inter-valence charge-transfer (IVCT) bands corresponding to Fe^{2+}–$Fe^{3+}(Ti^{4+})$-IVCT transitions [78]. They are located in the range for the single broad absorption band at ~18,000 cm^{-1}, which has been assigned to the $^{[6]}Fe^{2+}(M)\leftrightarrow{}^{[4]}Fe^{3+}(T_11)$ IVCT electronic transitions between adjacent M and T_11 sites [25,26] and reveal the polarization characteristics for the reported $^{[6]}Fe^{2+/3+}(M)\leftrightarrow{}^{[4]}Fe^{3+/2+}(T_11)$ or $^{[6]}Ti^{4+/3+}(M)\leftrightarrow{}^{[4]}Fe^{3+/2+}(T_11)$ IVCT transitions. The spectral changes related to the strong absorption in the UV region suggest F-centres to be responsible for the irradiation-induced changes. The study on natural radiohaloes [54] proposes the red-shift of the UV absorption edge to be related

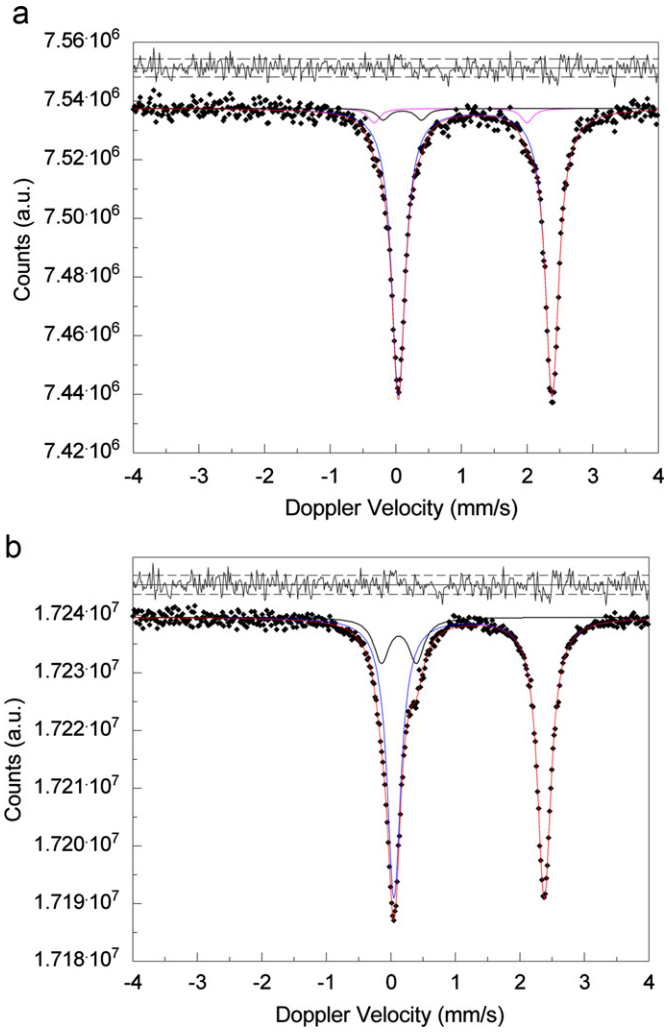

Fig. 3. Mössbauer spectra of powdered $(Mg_{0.879}Fe_{0.121})_2Al_4Si_5O_{18}$ samples (2.9 wt% FeO): (a) non-irradiated (sample Tsi1#R_n) and (b) irradiated with Ru ions (1×10^{12} cm^{-2}, sample Tsi1#C_ci).

to oxygen–metal charge transfer (OMCT) electronic transitions, explicitly due to oxygen–iron CT, which appears to be very likely considering the point-defect concentration to increase with irradiation. Possible mechanism for electron transfer might take into account the octahedral sites of Fe^{2+} and vacancies within the coordination sphere of the M site, thus suggesting $^{[6]}Fe^{2+}(M)+\square^{0}(O)\leftrightarrow{}^{[6]}Fe^{3+}(M)+{}^{e}\square^{-}(O)$ as one of the likeliest mechanism accounting for the suggested OMCT transitions. According to this, additional Fe^{2+} cations would have been involved for the release of free electrons, which in turn are trapped in the vacancies at the oxygen sublattice thus accounting for the F-centre. Simultaneously, the $Fe^{3+}/(Fe^{2+}+Fe^{3+})$ ratio increases, which in turn matches the interpretation of the Mössbauer spectra and corresponds to the relative changes of the ratio between ferric and ferrous iron. The presence of point defects with vacancies and interstitial positions has also been suggested by the luminescence background observed in Raman spectra, which scales with the fluence of ion exposure [57].

3.3. Irradiation effects on extra-framework channel species

The microporous nature of the cordierite framework was early recognized to reveal zeolite-like characteristics exhibiting open pores, which contain extra-framework atoms and molecular

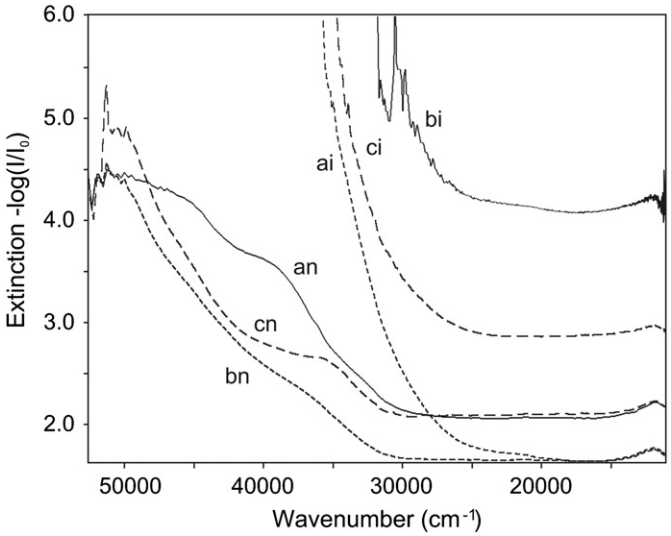

Fig. 4. Unpolarized optical absorption spectra in the wavenumber range 11,000 to 54,000 cm^{-1}, obtained for oriented crystal sections perpendicular to the crystallographic *a*-, *b*- and *c*-axis directions, non-irradiated samples (Tsi2#C_an, Tsi2#C_bn, Tsi2#C_cn) and samples irradiated with Au ions (1×10^{12} cm^{-2}) (Tsi2#C_ai, Tsi2#C_bi, Tsi2#C_ci). The irradiation was performed perpendicular to the surface of the 58–78 μm thick (100), (010) and (001) platelets.

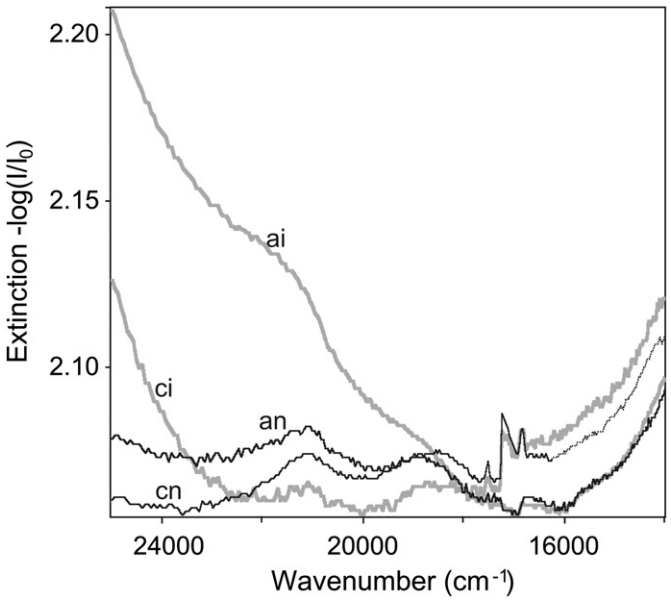

Fig. 5. Detail of the low wavenumber part of the spectra given in Fig. 4 between 15,000 and 25,000 cm^{-1} comparing the spectra obtained for the (100)-cut and (001)-cut samples (non-irradiated: an, cn; irradiated: ai, ci) in order to illustrate the three absorption bands (~18,300, ~21,200, ~22,000 cm^{-1}) assigned to charge transfer electronic transitions.

species such as H_2O and CO_2, but also N_2, Ar [30], CO [32,54–57], hydrocarbons [33,79–81], and possibly even molecular O_2 [82]. The librational motion due to dynamics of the molecule's rotational disorder [45,83,84] is typical of the dimensions of the one-dimensional open channels. The free diameter of the channels, which run parallel to the *c*-axis direction, varies between ~2.6 Å at the bottleneck (at $z=0$) and 5.4–6.0 Å at the centre of the cavities (at $z=0.25$).

The crystal structure investigations of the two samples in this study reveal significant differences for the extra-framework atoms within the channels. Nevertheless, difference-Fourier summations in both refinements give two maxima at 0,0,1/4 (=Ch1/4 site) and 0,0,0 (=Ch0 site), which were assigned to Na and to the oxygen atom (Ow) of the water molecules, respectively. The magnitude of the isotropic displacement parameters for Ow suggests both static and dynamic disorder of the H_2O molecule [83,84]. Bond lengths for the Na site are in good agreement with the previously reported stereochemistry, giving a [2+6] coordination by two Ow along the *c*-axis direction and laterally by 6 additional framework-oxygen atoms. The individual Na–$O_2$1, Na–$O_2$6, and Na–$O_2$3 bond distances correspond in both sample crystals perfectly to the site occupation of ~3–4% [39]. The most significant difference can be observed for the refined values of the site-occupancy factor (s.o.f.). While the s.o.f.'s for Na remain almost identical within the uncertainties of the refinements, the s.o.f.'s obtained for the Ow position in the irradiated crystal are remarkably smaller in comparison to the electron density on the Ch1/4 position in the non-irradiated sample. The irradiation-induced dehydration has already been described by Weikusat et al. [55], as observed from Raman intensities in line scans along the ion-penetration direction. The crystal-structure investigations here confirm that dehydration on irradiation is not complete, and a distinct amount of water is retained inside the channels and suggest all water molecules of class I, i.e. not bound to the Na atoms within the channels, to get expelled on irradiation. The findings give evidence for the residual water molecules to correspond to class II water, which is bound to the sodium atoms, and which cannot be removed from the coordination sphere of the Na atoms due to the strong Na–O bonding. Considering the two short Na–Ow distances (2.33 Å) and their bond-valence contributions of about 47%, the complete dehydration would require significant shortening of the Na–O bonds to the framework-oxygen atoms, which in turn would lead to a displacement of the Na atoms from the central Ch1/4 position. The electron-density maps derived from Fourier summations of X-ray intensities give no hint for such a displacement.

The Na contents are apparently not changed due to the irradiation as evidenced by the structure refinements. This is in contrast to the observations by Vance and Price [22], who report the loss of mobile charge carriers to coincide with a partial oxidation from Fe^{2+} to Fe^{3+}. Such a mechanism can be understood for charge compensation on assuming that thermal treatment does not involve the formation of vacancies. Nevertheless, as a consequence of the irradiation-induced dehydration, the dimensions of the channels shrink to some minor extent, which is associated with quasi-isotropic reduction of the whole lattice. The changes related to the decreasing water amount may be understood as a relaxation of the originally stuffed structure on removing extra-framework water molecules.

4. Conclusions

The exposure of $(Mg,Fe)_2Al_4Si_5O_{18}$ to high-energy heavy ions even to maximum fluences of 10^{13} ions/cm^2 was found to result in a surprisingly low degree of structural damage, and confirms the absence of amorphization, both on a local scale along ion trajectories and for bulk domains within the crystal. Basically undisturbed X-ray diffraction patterns give no evidence for a significant degradation of the long-range order within the $(Mg,Fe)_2Al_4Si_5O_{18}$ lattices, independent of the degree of (Mg,Fe) substitution. This is consistent with the findings from recent Raman spectroscopic investigations [55–57] reporting rather small intensity losses and almost insignificant broadening of vibrational-mode signals. The moderate irradiation effects can be associated with an increasing amount of point defects, which are the origin for the macroscopically observed radiocoloration.

The strong absorption in the blue region of the visible spectral range apparently accounts for the electronic transition between electrons in vacancies of the oxygen sublattice and the Fe centres. The presence of point defects with vacancies and interstitial positions has also been suggested from Raman spectroscopic investigations through the observed luminescence background, which scales with the fluence and the energy loss of the ions [57]. Mössbauer spectroscopy gives evidence for an increased amount of the Fe^{3+} fraction, most likely to be accommodated on the T_1 sites. Comparing the findings of this study using high-energy heavy ions to the investigations of natural radiohaloes [54], the radiation-induced structural alterations appear to be very similar and do not depend on the mass and energy of the ion species. Although relatively high ion fluences (10^{12} and 10^{13} ions/cm^2) were applied, the observed structural modifications suggest only moderate beam-induced temperature increase of the sample. The essentially unchanged cation distribution within the framework, in particular the undisturbed perfect ordering of Si and Al within the tetrahedral framework sites, clearly suggest that any heating of the sample during the irradiation must have been far below the critical temperature for the Al,Si order–disorder transition. Another clear indicator for only very modest thermal effects is the partial dehydration. As a consequence of the irradiation-induced dehydration, the dimensions of the channels shrink to some minor extent, which is associated with quasi-isotropic reduction of the whole lattice volume by about -0.2%. The changes related to the decreasing water amount may be understood as a relaxation of the originally stuffed structure on removing such an amount of extra-framework molecules. The apparently small changes in the lattice spacing for the individual direction appear to explain the formation of strain gradients across the interface between irradiated and non-irradiated domains and the subsequent loss of mechanical cohesion [55,57]. Once more, $(Mg,Fe)_2Al_4Si_5O_{18}$ attracts notice as an outstanding low-dielectric ceramics or ceramic-composite component due to the evident property of the material even to sustain large doses of high-energy particle radiation without significant degree of radiation damages and without loss of structural and mechanical coherence.

Acknowledgments

We acknowledge Marcus Schrauder, Vienna, for providing us with the three iolite specimens from Madagascar. We thank Ilona Fin and Oliver Wienand for their effort in careful preparation of the polished crystal sections, Sandra Panienka for her help with carrying out the SIMS analyses, Angela Ullrich for her assistance with the measurements on the Huber diffractometer, and Tim Seidel for his assistance during UV–vis spectrometry at GSI. We also like to thank Charles Geiger, Kiel, for valuable comments on an early version of the manuscript, and two anonymous reviewers for their critical comments. Financial support within the BMBF Verbundprojekt (project grant 05KK7VH1) and the GSI-Hochschulprojekt (project grant HDGLAS) is acknowledged.

Appendix A. Supplementary material

Supplementary data associated with this article can be found in the online version at doi:10.1016/j.jssc.2010.07.038.

References

[1] D.L. Evans, G.R. Fischer, J.E. Geiger, F.W. Martin, J. Am. Ceram. Soc. 63 (1980) 629.
[2] P.W. Mirwald, Phys. Chem. Miner. 7 (1981) 268–270.
[3] F.A. Hummel, Interceram 33 (1984) 27.
[4] S.S. Vepa, A.M. Umarji, J. Am. Ceram. Soc. 76 (1993) 1873–1876.
[5] R.R. Tummola, J. Am. Ceram. Soc. 74 (1991) 895.
[6] D.K. Agarwar, Y. Mehotra, V.S. Stubican, Opt. Eng. 25 (1986) 513.
[7] D.T. Weaver, F.S. Miller, D.C. Van Aken, J.D. Smith, in: Proceedings of the International Thermal Spray Conference, 2000, pp. 829–835.
[8] J.J. Liu, B. Zuberi, R.A. Dahl, W.M. Carty, US Patent Appl. 2009000260, 2009.
[9] J.J. Liu, B. Zuberi, J.G. Weinstein, R.A. Dahl, W.M. Carty, US Patent Ser. No. 11/753001, 2007.
[10] G.V. Gibbs, Am. Mineral. 51 (1966) 1068–1087.
[11] K. Langer, W. Schreyer, Am. Mineral. 54 (1969) 1442–1459.
[12] A. Putnis, Nature 287 (1980) 128–131.
[13] S.A.T. Redfern, E.K.H. Salje, W. Maresch, W. Schreyer, Am. Mineral. 74 (1989) 1293–1299.
[14] P. Daniels, B. Wunder, K. Sahl, W. Schreyer Eur., J. Mineral. 6 (1994) 323–335.
[15] E.P. Meagher, G.V. Gibbs Canad, Mineral 15 (1977) 43–49.
[16] T. Armbruster, Neues Jahrb. Miner. Monatsh. (1985) 255–267.
[17] B. Güttler, E. Salje, A. Putnis, Phys. Chem. Mineral. 16 (1989) 365–373.
[18] W.C.K. Poon, A. Putnis, E. Salje, J. Phys.: Condens. Matter 2 (1990) 6361.
[19] G.H. Faye, P.G. Manning, E.H. Nickel, Am. Mineral. 53 (1968) 1174–1201.
[20] H. Pollak, Phys. Stat. Sol. B 74 (1976) K31–K34.
[21] D.S. Goldman, G.R. Rossmann, Am. Mineral. 62 (1977) 1144–1157.
[22] E.R. Vance, D.C. Price, Phys. Chem. Miner. 10 (1984) 200–208.
[23] I. Abs-Wurmbach, C. Boberski, S. Hafner, Fortschr. Mineral. 66 (1989) 1.
[24] C.A. Geiger, H. Rager, M. Czank, Contrib. Mineral. Petrol. 140 (2000) 344–352.
[25] C.A. Geiger, T. Armbruster, V. Khomenko, S. Quartieri, Am. Mineral. 85 (2000) 1255–1264.
[26] V.M. Khomenko, K. Langer, C.A. Geiger, Contrib. Mineral. Petrol. 141 (2001) 381–396.
[27] J. Cohen, F. Ross, G.V. Gibbs, Am. Mineral. 62 (1977) 67–78.
[28] T. Armbruster, F.D. Bloss, Nature 286 (1980) 140–141.
[29] T. Armbruster, F.D. Bloss, Am. Mineral. 67 (1982) 284–291.
[30] T. Armbruster, Phys. Chem. Miner. 12 (1985) 233–245.
[31] B.A. Kolesov, C.A. Geiger, Am. Mineral. 85 (2000) 1265–1274.
[32] V.M. Khomenko, K. Langer, Am. Mineral. 90 (2005) 1913–1917.
[33] V.M. Khomenko, K. Langer, Am. Mineral. 84 (1999) 1181–1185.
[34] P. Cerny, R. Chapman, W. Schreyer, L. Ottolini, P. Bottazzi, C. McCammon, Can. Mineral. 35 (1997) 167–173.
[35] C. Bertoldi, A. Proyer, D. Garbe-Schönberg, H. Behrens, E. Dachs, Lithos 78 (2004) 389–409.
[36] P. Daniels, Am. Mineral. 77 (1992) 407–411.
[37] T. Armbruster, W. Schreyer, J. Hoefs, Contrib. Mineral. Petrol. 81 (1982) 262–267.
[38] T. Armbruster, H.B. Bürgi, Fortschr. Mineral. 60 (Beih. 1) (1982) 37–39.
[39] T. Armbruster, Am. Mineral. 71 (1986) 746–757.
[40] I. Abs-Wurmbach, C. Boberski, S. Hafner, Fortschr. Mineral. 66 (1989) 1.
[41] T. Armbruster, Neues Jahrb. Mineral. Monatsh. (1985) 255–267.
[42] T.A. Bul'bak, G.Y. Shvedenkov, Eur. J. Mineral. 17 (2005) 829–838.
[43] T.A. Bul'bak, S.V. Shvedenkova, Dokl. Earth Sci. 419A (2008) 477–480.
[44] M.A. Carpenter, A. Putnis, A. Navrotsky, J.D.C. McConnell, Geochim. Cosmochim. Acta 47 (1983) 899–906.
[45] D.G. Carson, G.R. Rossman, R.W. Vaughan, Phys. Chem. Miner. 8 (1982) 14–19.
[46] P. Daniels, Z. Kristallogr. 190 (1990) 276.
[47] P. Daniels, B. Wunder, K. Sahl, W. Schreyer, Eur. J. Minerals 6 (1994) 323–335.
[48] K. Langer, W. Schreyer, Am. Mineral. 61 (1976) 1036–1040.
[49] T. Malcherek, M.C. Domeneghetti, V. Tazzioli, L. Ottolini, C. McCammon, M.A. Carpenter, Am. Mineral. 86 (2001) 66–79.
[50] P.W. Mirwald, W.V. Maresch, W. Schreyer, Fortschr. Mineral. 57 (Beih. 1) (1979) 101–102.
[51] A. Putnis, Contrib. Mineral. Petrol. 74 (1980) 135–141.
[52] A. Putnis, E.K.H. Salje, S.A.T. Redfern, C. Fyfe, H. Stroble, Phys. Chem. Minerals 14 (1987) 446–455.
[53] E.K.H. Salje, Phys. Chem. Minerals 14 (1987) 456–466.
[54] L. Nasdala, M. Wildner, R. Wirth, N. Groschopf, D.C. Pal, A. Möller, Miner. Petrol. 86 (2006) 1–27.
[55] C. Weikusat, U.A. Glasmacher, R. Miletich, R. Neumann, C. Trautmann, Nucl. Instrum. Phys. Res. B 266 (2008) 2990–2993.
[56] R. Krickl, L. Nasdala, M. Wildner, D. Grambole, in: 86th Annual Meeting of the German Mineralogical Society, Berlin, Germany, Book of Abstracts, 2008, no. 210 (abstr.).
[57] C. Weikusat, R. Miletich, U.A. Glasmacher, C. Trautmann, R. Neumann, Phys. Chem. Minerals 37 (2010) 417–424.
[58] J.L. Pouchou, F. Pichoir, in: J.T. Armstrong (Ed.), Microbeam Analysis, 1985, pp. 104–106.
[59] N.J.G. Pearce, W.T. Perkins, J.A. Westgate, M.P. Gorton, S.E. Jackson, C.R. Neal, S.P. Chenery, Geostandards Newslett. 21 (1997) 115–144.
[60] R. Kaindl, P. Tropper, I. Deibl, Eur. J. Mineral. 18 (2006) 331–335.
[61] J.F. Ziegler, J.P. Biersack, U. Littmark, in: J.F. Ziegler (Ed.), The Stopping and Range of Ions in Matter, vol. 1, Pergamon Press, New York, 1985.
[62] H.E. King, L.W. Finger, J. Appl. Crystallogr. 12 (1979) 374–378.
[63] R.J. Angel, R.T. Downs, L.W. Finger, High-temperature and high-pressure crystal chemistry, in: R.M. Hazen, R.T. Downs (Eds.), Rev. Mineral. Geochem., 41, 2000, p. 559.
[64] CrysAlis Software system, Oxford Diffraction Ltd., Xcalibur CCD system, 2009.
[65] G.M. Sheldrick, in: SHELX-97. Programs for crystal structure determination and refinement, University of Göttingen, Germany, 1997.

[66] A.J.C. Wilson, E. Price, in: International Tables for Crystallography, vol. C, Kluwer Academic Publishers, Dordrecht, The Netherlands, 1999.
[67] N.E. Brese, M. O'Keeffe, Acta Crystallogr. B 47 (1991) 192–197.
[68] D.G. Rancort, J.Y. Ping, Nucl. Instrum. Methods B 58 (1991) 85–97.
[69] D.G. Rancourt, A.M. McDonald, A.E. Lalonde, J.Y. Ping, Am. Mineral. 78 (1993) 1–7.
[70] M. Toulemonde, S.M.M. Ramos, H. Bernos, C. Clerc, B. Canut, J. Chaumon, C. Trautmann, Nucl. Instrum. Methods B 178 (2001) 331.
[71] C. Trautmann, M. Boccanfuso, A. Benyagoub, S. Klaumünzer, K. Schwartz, M. Toulemonde, Nucl. Instrum. Methods B 191 (2002) 144–148.
[72] S.X. Wang, L.M. Wang, R.C. Ewing, R.H. Doremus, J. Non-Cryst. Solids 238 (1998) 198.
[73] W.E. Lee, T.E. Mitchell, A.H. Heuer, Radiat. Eff. 97 (1986) 115–126.
[74] K.R. Selkregg, F.D. Bloss, Am. Mineral. 65 (1980) 522–533.
[75] W. Schreyer, H.S. Yoder, Neues Jahrb. Mineral. Abh. 101 (1964) 271–342.
[76] P. McMillan, A. Putnis, M.A. Carpenter, Phys. Chem. Minerals 10 (1984) 256–260.
[77] V.L. Vinograd, Phys. Chem. Minerals 23 (1996) 391–401.
[78] K. Langer, A.N. Platonov, S.S. Matsyuk, M. Wildner, Eur. J. Mineral. 14 (2002) 1027–1032.
[79] J.L. Zimmermann, Bull. Minér. 104 (1981) 325–338.
[80] A. Mottana, A. Fusi, B. Bianchi Potenza, R. Crespi, G. Liborio, Neues Jahrb. Mineral. Abh. 148 (1983) 181–199.
[81] V.M. Khomenko, K. Langer, Am. Mineral. 84 (1999) 1181–1185.
[82] R. Krickl, L. Nasdala, D. Grambole, R. Kaindl, Geophysical Research Abstract, vol. 11 (2009) EGU2009-2657-2, EGU General Assembly 2009 (abstr.).
[83] B. Winkler, V. Milman, M.C. Payne, Am. Mineral. 79 (1994) 200–204.
[84] B. Winkler, G. Coddens, B. Hennion, Am. Mineral. 79 (1994) 801–808.